Thin Solid Films 519 (2011) 5503–5510

Contents lists available at ScienceDirect

Thin Solid Films

journal homepage: www.elsevier.com/locate/tsf

Influence of Zr on structure, mechanical and thermal properties of Ti–Al–N

Li Chen [a,b,*], David Holec [a], Yong Du [b], Paul H. Mayrhofer [a]

[a] Department of Physical Metallurgy and Materials Testing, Montanuniversität Leoben, Leoben, 8700, Austria
[b] State Key Laboratory of Powder Metallurgy, Central South University, Changsha Hunan, 410083, China

ARTICLE INFO

Article history:
Received 17 October 2010
Received in revised form 28 March 2011
Accepted 29 March 2011
Available online 15 April 2011

Keywords:
Physical vapor deposition
Density functional theory
Hardness
Thermal analysis
Titanium aluminum zirconium nitride
X-ray diffraction
Scanning electron microscopy
Ti-Al-N

ABSTRACT

Multinary Ti–Al–N thin films are used for various applications where hard, wear and oxidation resistant materials are needed. Here, we study the effect of Zr addition on structure, mechanical and thermal properties of $Ti_{1-x}Al_xN$ based coatings under the guidance of ab initio calculations. The preparation of $Ti_{1-x-z}Al_xZr_zN$ by magnetron sputtering verifies the suggested cubic (NaCl-type) structure for x below 0.6–0.7 and $z \leq 0.4$. Increasing the Zr content from $z = 0$ to 0.17, while keeping x at ~0.5, results in a hardness increase from ~33 to 37 GPa, and a lattice parameter increase from 4.18 to 4.29 Å. The latter are in excellent agreement with ab initio data. Alloying with Zr also promotes the formation of cubic domains but retards the formation of stable wurtzite AlN during thermal annealing. This leads to high hardness values of ~40 GPa over a broad temperature range of 700–1100 °C for $Ti_{0.40}Al_{0.55}Zr_{0.05}N$. Furthermore, Zr assists the formation of a dense oxide scale. After 20 h exposure in air at 950 °C, where $Ti_{0.48}Al_{0.52}N$ is already completely oxidized, only a ~1 μm thin oxide scale is formed on top of the otherwise still intact ~2.5 μm thin film $Ti_{0.40}Al_{0.55}Zr_{0.05}N$.

1. Introduction

Components like valves, tappets, and camshafts used in automotive industry, as well as tools for advanced machining processes (e.g., high-speed and dry cutting) are exposed to severe tribological and thermal conditions. Aluminum based ternary transition metal nitrides Me–Al–N hard coatings (e.g., Ti–Al–N, Cr–Al–N, and Zr–Al–N) with cubic NaCl (c) structure, where Al substitutes for Me in the MeN based lattice (i.e., $Me_{1-x}Al_xN$), are in favor for such industrial applications due to their high hardness and wear resistance, together with good thermal stability, and oxidation resistance [1–11]. Among them, Ti–Al–N coatings are the most widely used to reduce tool wear. The crystal structure and mechanical properties of Ti–Al–N are depending on the Al content. Single phase cubic Ti–Al–N films with high Al contents exhibit excellent mechanical properties, age-hardening and oxidation resistance. For Al contents exceeding the maximum solubility (AlN mole fraction x_{max} ~0.7, depending on the deposition conditions, see Ref. [12]) in the cubic phase, a mixed cubic-NaCl and wurtzite-ZnS (w-AlN) structure is formed. The wurtzite configuration exhibits lower hardness, bulk-, elastic-, and shear-moduli, as well as wear resistance [13–17].

High thermal stability and oxidation resistance of hard films are the key requirements of many industrial applications. Ti–Al–N films form a bi-layered Al_2O_3/TiO_2 oxide scale, if exposed to air at elevated temperatures [18,19]. The oxidation resistance of Ti–Al–N films, with a reported onset temperature for oxidation of up to ~850 °C [19], is a result of the formation of dense Al_2O_3 scales, which retard the corresponding diffusion processes (simultaneous outward diffusion of Al and inward diffusion of O). However, the high growth rate of porous TiO_2, when Ti–Al–N is exposed to temperatures exceeding 850 °C, results in crack formation also within the dense and protective Al_2O_3 outer-scale [18,19]. Consequently, break away oxidation occurs. In addition to the oxidation resistance also the age-hardening ability of Ti–Al–N films, which originates from spinodal decomposition to form cubic Al-rich and Ti-rich domains during annealing at temperatures below 1000 °C, [4–7,20] is attractive for industrial applications. Similar properties have led to the introduction of $Zr_{1-x}Al_xN$, where the reported metastable solubility limit for AlN in the c-$Zr_{1-x}Al_xN$ is at 42–47 mol% [9,10,21–23]. Annealing of c-$Zr_{1-x}Al_xN$ results in decomposing into their stable phases c-ZrN and w-AlN via the formation of cubic Al-rich domains and concomitant age-hardening up to an annealing temperature of 600 °C [21,22]. The transformation of the cubic Al-rich domains into the stable structure w-AlN for annealing treatments (or exposure during operation) above 1000 °C results in a rapid decline of the mechanical properties [4–6]. Furthermore, with increasing time of the exposure the corresponding transformation can occur already at lower temperatures.

Therefore, during severe industrial applications reaching or exceeding working temperatures of 1000 °C, or to increase the lifetime of these coatings, further optimization of the oxidation resistance and the thermal stability in general is needed. An improvement of their properties can be achieved by the incorporation of large (substitutional) atoms (e.g., Nb, Ta and Y) into Ti–Al–N [24–28], as

* Corresponding author. Tel.: +86 0731 888 36213.
E-mail address: chenli_927@126.com (L. Chen).

0040-6090/$ – see front matter © 2011 Elsevier B.V. All rights reserved.
doi:10.1016/j.tsf.2011.03.139

they effectively retard diffusional driven processes resulting in an increased thermal stability as well as improved mechanical properties. Alloying Zr to TiN and Ti–Al–N is reported to improve their hardness due to solid solution strengthening [29,30]. However, a detailed literature survey revealed that the impact of Zr incorporation on thermal stability and oxidation resistance of Ti–Al–N has not yet been explored.

In the present work we use differential scanning calorimetry (DSC), thermal gravimetric analysis (TGA), stress measurements, X-ray diffraction analysis (XRD), and nanoindentation measurements to investigate the thermal stability, structure evolution, and mechanical properties of magnetron sputtered Ti–Al–Zr–N films for annealing temperatures up to 1500 °C. The effect of Zr-incorporation on the oxidation resistance of Ti–Al–N films is studied by means of DSC measurements in synthetic air, subsequent XRD, and cross-sectional scanning electron microscopy (SEM) investigations of coated polycrystalline Al_2O_3 substrates after isothermal oxidation for 20 h at 850 and 950 °C.

For a better understanding and explanation of the observed results we use density function theory (DFT) to calculate the energy of formation, bulk moduli and lattice parameters of cubic and wurtzite modifications of the $Ti_{1-x-z}Al_xZr_zN$ solid solution with x between 0 and 1, and z between 0 and 0.3.

2. Experimental and calculation details

$Ti_{1-x-z}Al_xZr_zN$ films were deposited onto various substrates (see next paragraph) by unbalanced magnetron sputtering from a powder-metallurgically prepared $Ti_{0.5}Al_{0.5}$ compound target (diameter of 152 mm, thickness of 5 mm and purity of 99.9%, PLANSEE) in a mixed $Ar+N_2$ (both of 99.999% purity) glow discharge. $Ti_{1-x-z}Al_xZr_zN$ films with different compositions were obtained by placing Ti and Zr platelets on the target race track (diameter of 5 mm and thickness of 1 mm). Prior to the deposition with a constant substrate temperature (T_a) of 500 °C, a base pressure ≤0.8 mPa, a bias potential of −60 V, a N_2-to-total pressure ratio of 17%, and a substrate-to-target distance of 85 mm, the substrates were etched for 20 min using an Ar^+ glow discharge with −1250 V and 25 mA, at a pressure of 3.0 Pa. More details on the magnetron sputtering system used are given in Ref. [31].

Different substrates were used for the individual investigations: austenitic stainless steel for hardness measurements of as deposited films; polished MgO (100) plates ($10\times10\times1$ mm^3) for hardness measurements of as deposited and annealed films; Si stripes ($20\times7\times0.3$ mm³, both sides polished) for residual stress measurements; low alloyed steel for DSC and X-ray diffraction measurements of as deposited and annealed films and polycrystalline Al_2O_3 plates ($10\times10\times1$ mm3) for oxidation resistance measurements. Before loading the deposition chamber, the substrates were ultra-sonically cleaned in acetone and ethylene.

DSC with TGA was performed in a Netzch-STA 409C from room temperature (RT) to 1500 °C with a heating rate of 20 K/min in flowing He (99.9% purity and 20 sccm flow rate) and synthetic air (79% N_2, 21% O_2, and 20 sccm flow rate). Prior to these measurements, the Ti–Al–Zr–N films were removed from their low alloyed steel substrates by chemical etching in 10 mol% nitric acid, in order to avoid substrate interference. For isothermal oxidation experiments, coated polycrystalline Al_2O_3 substrates were isothermally oxidized at 850 and 950 °C for 20 h in a conventional tube furnace, and afterwards investigated by fracture cross-sectional scanning electron microscopy (SEM) studies.

The chemical compositions of the films in their as deposited state and after the oxidation experiments were determined using energy dispersive X-ray analysis (EDX) with an Oxford Instruments INCA EDX unit attached to a SEM operated with 25 kV. The error of measurements for the metal atoms is below 2 at.%. Phase identification and structural investigations of the layers (after removal from their low alloy steel substrates) in their as deposited state and after thermal treatment with the DSC equipment in He or synthetic air were conducted by XRD with CuK_α radiation using a Brucker D8 diffractometer in Bragg/Brentano mode. For classification of XRD peak, the JCDPS database was used [32]. Nanoindentation measurements of as deposited films and after vacuum annealing to 1100 °C were conducted with a CSIRO ultra-micro-indentation system (UMIS) using a Berkovich indenter. With respect to a proper statistic, at least 30 indents were performed for each sample with maximum loads ranging from 8 to 30 mN. Hardness and indentation moduli were calculated from the loading and unloading curves employing the Oliver–Pharr method [33]. Residual stresses σ of as deposited films were obtained using the substrate-curvature method. Detailed information on the measurement and the calculation of σ is described in Ref. [34].

Vacuum annealing of our films on MgO substrates was conducted in a vacuum furnace (pressure ≤0.1 mPa) to temperatures up to $T_a = 1100$ °C, using a heating rate of 20 K/min (corresponding to the DSC measurements).

DFT calculations were performed using the VASP code [35] and employing the projector augmented wave pseudopotentials based on the generalized gradient approximation as parametrized by Perdew and Wang [36]. We used 500 eV for the plane wave cut-off energy and approximately 320 k-points/atom. Such parameters guarantee the calculation accuracy in the order of meV/atom. Special quasi-random structure (SQS) [37] based supercells ($3\times3\times2$ (36 atoms) for the cubic and $2\times2\times2$ (32 atoms) for the wurtzite modification) were generated to model the ternary and quaternary alloys. This methodology allows to randomize the Ti and Al atoms on the metallic sublattice with respect to their short-range order (SRO) parameters. We used our own scripts for generating the supercells which are in detail described for the wurtzite phase elsewhere [38]. The resulting supercells used for the calculations in the present work are summarized in Appendix A (Tables A1 and A2). The deviation from ideal random-like behavior can be quantified by Warren–Cowley SRO parameters which are given in Table A3 in Appendix A. One can see that compared with a similar approach by Alling et al. [39], our cells exhibit in general worse SRO parameter values. This is likely to be cased by using considerably smaller supercells (36 and 32 atoms in the cubic and wurtzite phase, respectively compared with 64 atoms used by Alling et al. to model the cubic structure [39]). Nevertheless, even these rather small supercells have proved to be able to provide useful information on the structure and energetics of other similar ternary systems [40,41]. To obtain quaternary alloys we replaced one or two Ti or Al atoms by Zr. Thereby, we obtained cubic $Ti_{1-x-z}Al_xZr_zN$ structures with $z=0.056$ and 0.111, and wurtzite $Ti_{1-x-z}Al_xZr_zN$ structures with $z=0.0625$ and 0.125. Additionally, we also optimized an ad hoc cubic $Ti_{0.33}Al_{0.39}Zr_{0.28}N$ structure (the metal sublattice is composed of 6 Ti, 7 Al, and 5 Zr atoms).

3. Results and discussion

3.1. Structure and mechanical properties

Elemental analysis by EDX reveals that our $Ti_{1-x-z}Al_xZr_zN$ films are stoichiometric with N/metal ratios of 1 ± 0.1. As mentioned in the experimental section the composition of the metal sublattice is varied by adding Ti or Zr platelets at the race track of the $Ti_{0.5}Al_{0.5}$ compound target. Thereby the following films are obtained: $Ti_{0.48}Al_{0.52}N$ with 21 Ti platelets, $Ti_{0.40}Al_{0.55}Zr_{0.05}N$ with 10 Zr platelets, $Ti_{0.39}Al_{0.51}Zr_{0.10}N$ with 20 Zr platelets, $Ti_{0.36}Al_{0.47}Zr_{0.17}N$ with 40 Zr platelets, and $Ti_{0.34}Al_{0.37}Zr_{0.29}N$ with 80 Zr platelets. XRD investigations of these as deposited films, as shown in Fig. 1, reveal a single phase cubic structure, which is in agreement with ab initio calculations. Fig. 2a presents the energy of formation, E_f, of the cubic and wurtzite

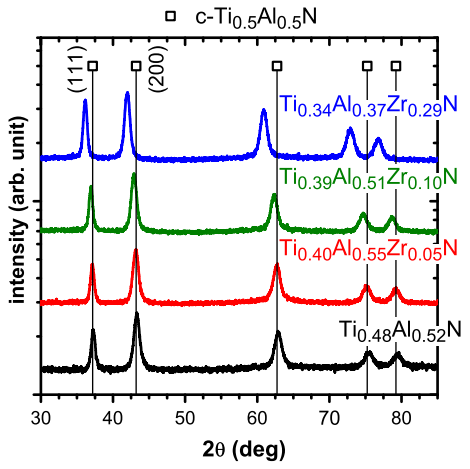

Fig. 1. XRD patterns of as deposited powdered $Ti_{1-x-z}Al_xZr_zN$ thin films.

$Ti_{1-x-z}Al_xZr_zN$ alloys with constant z = 0, 0.05 and 0.1 as a function of the AlN mole fraction x. The data suggest a transition from cubic to wurtzite structure $Ti_{1-x-z}Al_xZr_zN$ at x ~0.72, 0.70, and 0.68 for a ZrN mole fraction z of 0, 0.05, and 0.10, respectively. Since the compositional steps given by the supercell sizes are different for the cubic (1/18) and for the wurtzite (1/16) alloys, to evaluate the maximum solubility of AlN in the cubic phase we proceeded as follows. First, we fitted each set of data with constant ZrN mole fraction with a third order polynomial $(a_0 + a_1 \cdot x + a_2 \cdot x^2 + a_3 \cdot x^3)$. For c-$Ti_{1-x-z}Al_xZr_zN$, the AlN mole fraction x was varied 19 times for z = 0, 12 times for z = 0.055, and 10 times for z = 0.111. The calculations of

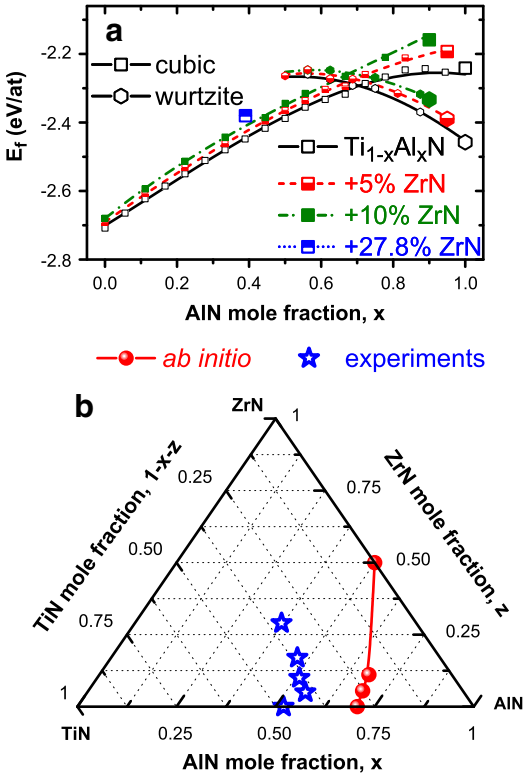

Fig. 2. (a) Energy of formation, E_f, for c-$Ti_{0.33}Al_{0.39}Zr_{0.28}N$ and cubic and wurtzite phases $Ti_{1-x-z}Al_xZr_zN$ with z = 0, 0.05 and 0.1 as functions of AlN mole fraction. (b) Overall chemical compositions of our $Ti_{1-x-z}Al_xZr_zN$ films, in the as deposited state, plotted within the TiN–AlN–ZrN quasi-ternary phase diagram. The solid line indicates the transition between preferred cubic and wurtzite phases.

w-$Ti_{1-x-z}Al_xZr_zN$ were obtained with 7, 6, and 5 variations in x for z = 0, 0.0625, and 0.125, respectively, in the composition range x = 0.5–1. Subsequently, for each phase (i.e. cubic or wurtzite) we fitted individually the coefficients (i.e., a_0, a_1, a_2, and a_3) of their third order polynomial for the three different ZrN mole fractions, z, with a linear expression in the ZrN contents. This way, two polynomial fits (one for the cubic and one for the wurtzite modification) as functions of x (AlN mole fraction) and z (ZrN mole fraction) were obtained. In the last step, we used these fits to estimate the cross-over between the formation energies of the cubic and wurtzite phases at fixed ZrN mole fractions (and thus to estimate the influence of Zr on the maximum AlN mole fraction in the cubic $Ti_{1-x-z}Al_xZr_zN$). Fig. 2b shows this transition with a solid line connecting the data points (circles) as obtained for $Ti_{1-x-z}Al_xZr_zN$ with z = 0, 0.05, and 0.1 and ZrN-AlN, in the quasi-ternary TiN-AlN-ZrN diagram. It is worth noting, that the calculated transition point (maximum Al content in the cubic phase) is not too sensitive to a chosen order of the fitting polynomials: it ranges from 0.72 ($z = 0$) to 0.67 ($z = 0.11$) when using quadratic fits, from 0.705 ($z = 0$) to 0.68 ($z = 0.11$) for the third order polynomial, and from 0.70 ($z = 0$) to 0.68 ($z = 0.11$) for the fifth order polynomials. The chemical composition of our deposited films (indicated by asterisks) are deep within the single phase cubic region and hence in agreement to the XRD results. Additionally, we calculated the cubic-to-wurtzite transition for $Zr_{1-z}Al_zN$ alloy to be ~0.5.

The shift of the XRD peak positions to lower 2θ angles indicate increasing lattice parameters from 4.18 to 4.19 to 4.23 to 4.31 Å with increasing ZrN mole fraction z for the films $Ti_{0.48}Al_{0.52}N$, $Ti_{0.40}Al_{0.55}Zr_{0.05}N$, $Ti_{0.39}Al_{0.51}Zr_{0.10}N$, and $Ti_{0.34}Al_{0.37}Zr_{0.29}N$, respectively. These lattice parameters, obtained from powdered film samples after removing from their low alloy steel substrates, are in excellent agreement (maximum deviation of 0.2%) with the ab initio obtained lattice parameters of a = 4.184, 4.197, 4.238, and 4.320 Å for $Ti_{0.50}Al_{0.50}N$, $Ti_{0.389}Al_{0.556}Zr_{0.056}N$, $Ti_{0.389}Al_{0.50}Zr_{0.111}N$, and $Ti_{0.33}Al_{0.39}Zr_{0.28}N$. Fig. 1 furthermore shows that the 111/200 peak intensity increases with increasing Zr content for the samples $Ti_{0.40}Al_{0.55}Zr_{0.05}N$, $Ti_{0.36}Al_{0.47}Zr_{0.17}N$, and $Ti_{0.34}Al_{0.37}Zr_{0.29}N$, which is in agreement to our previous studies [3,16] and other reports [4,42] suggesting that with increasing Al content the 200 orientation is preferred. Stress measurements by the substrate-curvature method of films on Si substrates suggest increasing compressive stresses from around −1.45 to −3.53 GPa with increasing ZrN mole fractions z from 0 to 0.29, see Fig. 3.

The nanoindentation obtained values for hardness H and indentation moduli E of our $Ti_{1-x-z}Al_xZr_zN$ films are also presented as a function of their ZrN mole fraction in Fig. 3. While the compressive stresses scale with the ZrN mole fraction the maximum H and E values

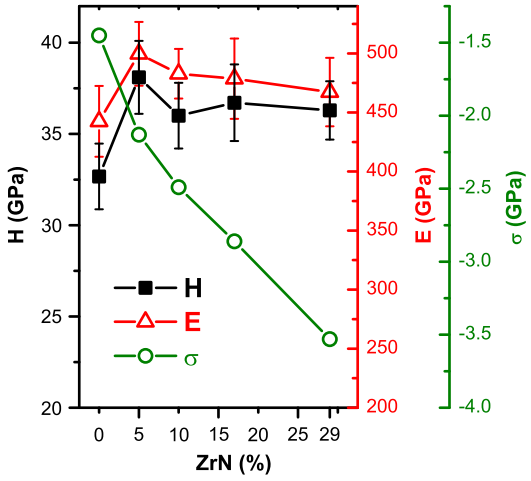

Fig. 3. Hardness, H, indentation modulus, E, and residual stresses, σ, of $Ti_{1-x-z}Al_xZr_zN$ films as a function of z.

of ~38.1 and 499.7 GPa are obtained for the $Ti_{0.40}Al_{0.55}Zr_{0.05}N$ film which contains 5 mol% ZrN. A further increase in Zr content results in lower hardness values of ~36.0, 36.7, and 36.3 GPa for 10, 17, and 29% ZrN, respectively. This is connected with a decrease in the Al content and hence a decrease in the covalent character of bonding in the films [12], as the overall structure (see the XRD patterns presented in Fig. 1) and columnar morphology (not shown here) of the coatings are very similar. Nevertheless, the hardness values for the $Ti_{0.36}Al_{0.47}Zr_{0.17}N$ and $Ti_{0.34}Al_{0.37}Zr_{0.29}N$ films are by ~3–4 GPa above the hardness of ~32.7 GPa from the Zr-free reference film $Ti_{0.48}Al_{0.52}N$, which has a higher Al content. Consequently, Zr is very effective in increasing the strength of the materials. The indentation moduli E first increases from ~443 GPa for $Ti_{0.48}Al_{0.52}N$ to 500 GPa for $Ti_{0.40}Al_{0.55}Zr_{0.05}N$ and then slightly decreases to 467 GPa for $Ti_{0.34}Al_{0.37}Zr_{0.29}N$ with increasing Zr, see Fig. 3. Ab initio calculations suggest a decrease in bulk moduli by ~6 and 12 GPa by the addition of z = 0.055 and 0.111 ZrN to c-$Ti_{1-x}Al_xN$ to form c-$Ti_{1-x-z}Al_xZr_zN$, respectively. In particular the calculated bulk moduli of $Ti_{0.45}Al_{0.55}N$, $Ti_{0.395}Al_{0.55}Zr_{0.055}N$, $Ti_{0.339}Al_{0.55}Zr_{0.111}N$, and $Ti_{0.33}Al_{0.39}Zr_{0.28}N$ are 261, 255, 249, and 245 GPa, respectively. Consequently, the experimentally observed rapid increase in H and E when adding 5% ZrN to $Ti_{1-x}Al_xN$ is mainly attributed to microstructural changes.

3.2. Thermal stability

Fig. 4 shows simultaneous thermal analysis results of our $Ti_{1-x-z}Al_xZr_zN$ films, combining DSC (Fig. 4a) and TGA (Fig. 4b). The base line corrected dynamical DSC signal between 400 and 1500 °C consists of exothermic features from irreversible reactions. The shape of the broad DSC feature in the temperature range between 500 and 1100 °C suggests the contribution of several exothermic reactions for all films investigated, according to the results presented in Ref. [5]. With increasing ZrN mole fraction from 0 to 0.05 to 0.10 the peak position decreases from 800 °C for $Ti_{0.48}Al_{0.52}N$ to 760 °C for $Ti_{0.4}Al_{0.55}Zr_{0.05}N$ to 740 °C for $Ti_{0.39}Al_{0.51}Zr_{0.1}N$. However, a further increase of Zr content to z = 0.29 ($Ti_{0.34}Al_{0.37}Zr_{0.29}N$) again results in a higher peak temperature of ~845 °C of this overall exothermic feature. For the exothermic feature at temperatures above 1100 °C, a shift in peak temperature from 1210 °C for $Ti_{0.48}Al_{0.52}N$ to 1280 °C for $Ti_{0.34}Al_{0.37}Zr_{0.29}N$ is obtained with the incorporation of Zr. TGA measurements of these films indicate a decreasing mass loss of ~0.9, 0.6, 0.5 and 0.0% with increasing Zr content during annealing up to 1500 °C, see Fig. 4b. Based on previous studies, see Ref. [24], the mass loss can be correlated with N_2-release, here, 1% mass loss corresponds to less than ~2 at.% N. Hence, the contribution to the exothermic output during DSC is mainly given by the decomposition of the metastable solid solution into their 'stable' nitrides, recovery and recrystallization. Ab initio obtained mixing enthalpies (from the binary constituents c-TiN, c-ZrN, and w-AlN) for c-$Ti_{0.48}Al_{0.52}N$, c-$Ti_{0.4}Al_{0.55}Zr_{0.05}N$, c-$Ti_{0.39}Al_{0.51}Zr_{0.1}N$, and c-$Ti_{0.34}Al_{0.37}Zr_{0.29}N$ are 104, 116, 119, and 120 meV/at, respectively, and hence increase with increasing ZrN content. When using a cubic solid solution between TiN and ZrN, i.e. c-$Ti_{1-y}Zr_yN$ (with y = z/(1-x)) as a constituent next to w-AlN, we obtain mixing enthalpies of 104, 98, 87, and 72 meV/at for z = 0, 0.05, 0.10, and 0.29, respectively. In Ref. [43] it is reported that TiN and ZrN forms a solid solution, which is stable up to at least 1200 °C during thermal annealing in vacuum for 2 h, and which also exhibits almost no exothermic contribution during DSC. The latter reference and the comparison of the mixing enthalpies with the DSC experiments, which exhibit an overall exothermic contribution of 192, 232, 227, and 140 W·K/g for the coatings c-$Ti_{0.48}Al_{0.52}N$, c-$Ti_{0.4}Al_{0.55}Zr_{0.05}N$, c-$Ti_{0.39}Al_{0.51}Zr_{0.1}N$, and c-$Ti_{0.34}Al_{0.37}Zr_{0.29}N$, suggests (by the overall trend of decreasing enthalpies with increasing Zr content) that there is no separation into the constituents c-TiN, c-ZrN, and w-AlN (increasing mixing enthalpies with increasing Zr) but into c-$Ti_{1-y}Zr_yN$ and w-AlN (decreasing mixing enthalpies with increasing Zr), see above. This is verified by XRD analysis of samples annealed to various temperatures using the DSC equipment with the same setup, atmosphere, heating and cooling rates.

Fig. 5 shows the structural evolution during annealing of our $Ti_{0.48}Al_{0.52}N$ (a) $Ti_{0.4}Al_{0.55}Zr_{0.05}N$ (b) and $Ti_{0.39}Al_{0.51}Zr_{0.1}N$ (c) films by means of XRD patterns after annealing to 700, 850, 1100, 1200, and 1500 °C. The Zr-free $Ti_{0.48}Al_{0.52}N$ film exhibits a small shift of the XRD peaks during annealing to 700 °C as compared with the as deposited state, see Fig. 5a, suggesting only minute structural changes like recovery and relaxation which contribute to the exothermic DSC feature in this temperature range. The XRD patterns of the Zr-containing films $Ti_{0.4}Al_{0.55}Zr_{0.05}N$ and $Ti_{0.39}Al_{0.51}Zr_{0.1}N$ annealed to 700 °C reveal also a shift in the peak position to higher diffraction angles but also an increase in peak broadening, see Fig. 5b and c. The latter is an indication for a reduction in grain size and/or an increase in microstresses which can result from the onset of a decomposition process [14,20]. This can better be seen after annealing at 850 °C, where the XRD peaks exhibit on both sides (lower and higher diffraction angles) an increase in intensity and width, suggesting the formation of Al-depleted and Al-enriched domains. After annealing at 1100 °C, a pronounced shoulder-formation on both sides of the 'matrix' XRD peak can be seen clearly. These shoulders indicate the

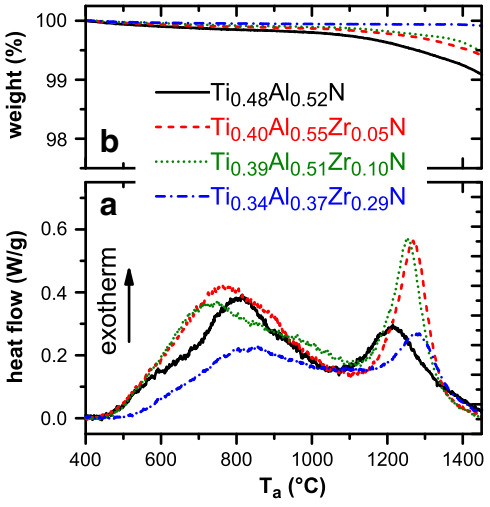

Fig. 4. (a) DSC and (b) TGA scans in inert atmosphere (He) of our $Ti_{1-x-z}Al_xZr_zN$ thin films.

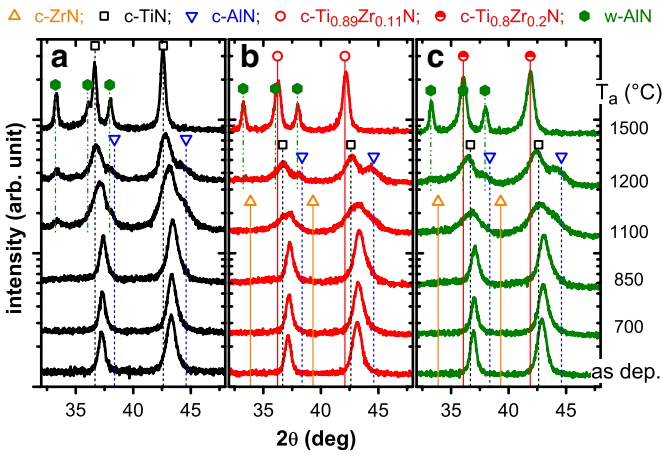

Fig. 5. XRD patterns after annealing in vacuum to temperatures T_a up to 1500 °C of (a) $Ti_{0.48}Al_{0.52}N$, (b) $Ti_{0.40}Al_{0.55}Zr_{0.05}N$, and (c) $Ti_{0.39}Al_{0.51}Zr_{0.10}N$.

formation of TiN- and AlN-rich cubic domains for $Ti_{0.48}Al_{0.52}N$, and TiN-, ZrN- and AlN-rich cubic domains for the Zr-containing films. While the Zr-free film, $Ti_{0.48}Al_{0.52}N$, exhibits the formation of w-AlN already after annealing at 1100 °C, no w-AlN formation can be detected for the Zr-containing films (compare Fig. 5a, b, and c), indicating that Zr effectively retards the formation of w-AlN. After annealing at 1200 °C, almost no intensity at the XRD peak positions of as deposited films can be detected, indicating close-to-complete decomposition of the original supersaturated matrix. The $Ti_{0.48}Al_{0.52}N$ film is mainly composed of TiN- and AlN-rich cubic phases and w-AlN, whereas it is still hard to detect any w-AlN for the Zr containing films, $Ti_{0.4}Al_{0.55}Zr_{0.05}N$ and $Ti_{0.39}Al_{0.51}Zr_{0.1}N$, which at this stage compose mainly of ZrN-, TiN- and AlN-rich cubic phases.

Increasing the temperature further to 1500 °C results in a completed decomposition to form the stable counterparts c-TiN and w-AlN for the Zr-free film, and c-$Ti_{1-y}Zr_yN$ and w-AlN for the Zr-containing films, see Fig. 5. The development of the XRD patterns of the Zr-containing films with temperature suggests that the TiN and ZrN rich cubic domains, formed at temperatures below 1200 °C, combine to form the solid solution c-$Ti_{1-y}Zr_yN$ phases present after annealing at 1500 °C. The obtained cubic phases of $Ti_{0.89}Zr_{0.11}N$ and $Ti_{0.80}Zr_{0.20}N$ have lattice parameters a = 4.28 and 4.31 Å, respectively. This behavior is further studied with the structural development of the higher Zr containing film $Ti_{0.34}Al_{0.37}Zr_{0.29}N$ as a function of annealing temperature, see Fig. 6. The XRD patterns after annealing at 850, 950 and 1100 °C suggest the formation of cubic structure ZrN-, TiN- and AlN-rich domains. The small peaks at the positions for c-TiN and c-ZrN move towards c-$Ti_{0.54}Zr_{0.46}N$ (a = 4.39 Å) with a further increase in temperature to 1200, 1300 and 1500 °C. The formation of w-AlN can only be detected for $T_a \geq 1300$ °C, see the small peaks at 2θ = 33.2 and 38.2°.

The structural changes occurring in the films during annealing result in corresponding changes of their mechanical properties. The hardness values of our $Ti_{1-x-z}Al_xZr_zN$ films for annealing temperatures T_a up to 1100 °C are presented in Fig. 7. The hardness of $Ti_{0.48}Al_{0.52}N$ slightly decreases from ~31.9 to 31.4 GPa, within the error of the measurement of ±1.5 GPa, during annealing to 700 °C. The previous structural investigations indicate that in this temperature range mainly recovery and relaxation processes occur, which can explain the small change in H. With a further increase in T_a, and hence the onset of the decomposition of the supersaturated cubic matrix to form cubic domains, the hardness increases to ~34.7 GPa with T_a = 1000 °C. The formation of w-AlN and coarsening of individual phases during annealing to 1100 °C leads to a decrease in H to ~30.3 GPa (compare Figs. 7 and 5). The 5 mol% ZrN containing film $Ti_{0.40}Al_{0.55}Zr_{0.05}N$ exhibits an almost steady increase in H from the as deposited value of 37.7 ± 2.6 GPa to 42.0 ± 2.3 GPa with T_a = 1000 °C within the error of measurement. After annealing at 1100 °C the hardness only slightly decreased to 39.7 ± 1.8 GPa. The higher Zr containing film $Ti_{0.39}Al_{0.51}Zr_{0.1}N$ shows also an increase in H from the as deposited value of 33.5 ± 2.0 GPa to 37.0 ± 2.7 GPa with T_a = 900 °C. A further increase in T_a results in a decrease of H to 34.6 ± 2.5 GPa at T_a = 1100 °C. Consequently, the higher Zr containing film reaches its peak hardness already at 900 °C. The earlier increase in hardness followed by a later decrease with increasing temperature is consistent with the structural investigations indicating an earlier onset of the decomposition process to form cubic domains but postponed formation of w-AlN for the Zr containing films as compared with $Ti_{0.48}Al_{0.52}N$, see Figs. 5 and 6.

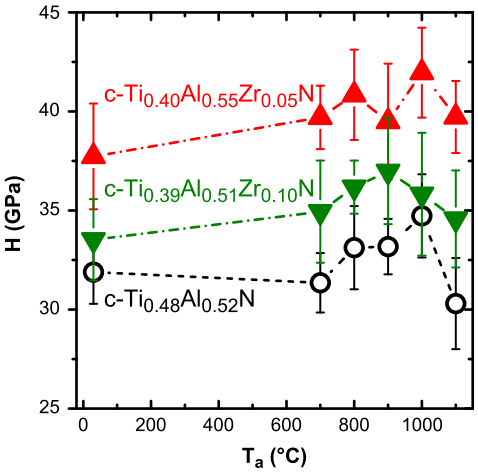

Fig. 7. Hardness, H, of $Ti_{1-x-z}Al_xZr_zN$ layers on MgO (001) as a function of T_a.

3.3. Oxidation resistance

Fig. 8 shows the results of dynamical DSC experiments of powdered freestanding film samples up to 1500 °C in synthetic air, allowing for a qualitative comparison of the temperatures where distinct reactions occur. The $Ti_{0.34}Al_{0.37}Zr_{0.29}N$ film shows the lowest onset temperature (~800 °C) of exothermic heat flow of the films investigated, which is

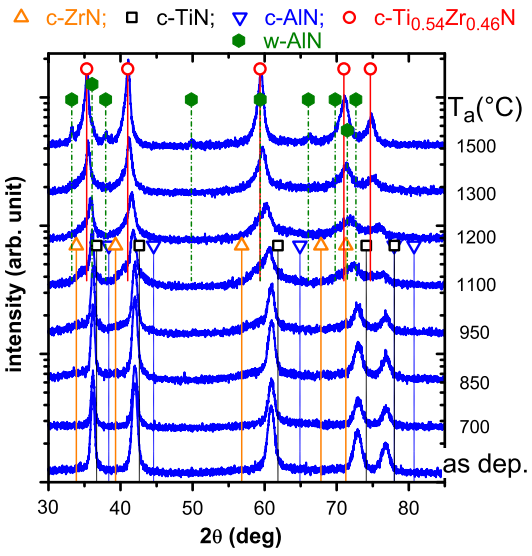

Fig. 6. XRD patterns of $Ti_{0.34}Al_{0.37}Zr_{0.29}N$ after annealing in vacuum to temperatures T_a up to 1500 °C.

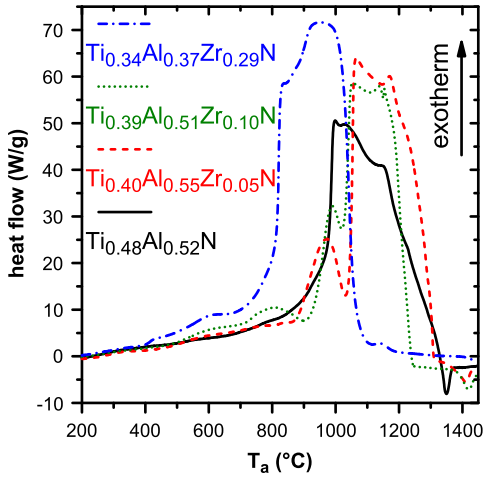

Fig. 8. DSC spectra of powdered $Ti_{1-x-z}Al_xZr_zN$ films in synthetic air (20 sccm) with a 20 K/min heating rate.

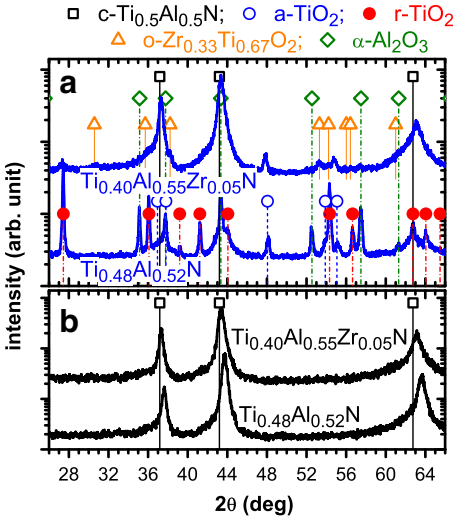

Fig. 9. XRD scans of $Ti_{0.48}Al_{0.52}N$ and $Ti_{0.40}Al_{0.55}Zr_{0.05}N$ after (a) annealing at 1000 °C in synthetic air (20 sccm) for 1 h, and (b) vacuum annealing to 950 °C with a 20 K/min heating rate (b).

mainly attributed to the low Al content (x ~0.37) and the high amount of Zr, which is highly affine to O_2. The other films with a higher Al content (x ~0.5) exhibit the pronounced oxidation reaction at temperatures above 1000 °C with the Zr-containing films exhibiting an additional pre-reaction in the temperature range 870–1030 °C. The latter can especially be observed for $Ti_{0.40}Al_{0.55}Zr_{0.05}N$. The XRD analyses of $Ti_{0.48}Al_{0.52}N$ and $Ti_{0.40}Al_{0.55}Zr_{0.05}N$ freestanding films after annealing in ambient air at 1000 °C for 1 h, Fig. 9a, indicate that $Ti_{0.48}Al_{0.52}N$ is almost completely oxidized to form rutile, r-TiO_2, (with some anatase, a-TiO_2,) and α-Al_2O_3. On the contrary, the XRD pattern of $Ti_{0.40}Al_{0.55}Zr_{0.05}N$ after annealing in air is very similar to that after annealing in vacuum, Fig. 9b, and only small XRD peaks, suggesting the formation of TiO_2, α-Al_2O_3, and $Zr_{0.33}Ti_{0.67}O_2$ can be detected. Consequently, the pre-reaction to the strong exothermic contribution during DSC of $Ti_{0.40}Al_{0.55}Zr_{0.05}N$ (Fig. 8) is assigned to the formation of stable oxides which slow down a further oxidation.

Fig. 10 shows back scattered SEM fracture cross sections of $Ti_{0.48}Al_{0.52}N$ (a), $Ti_{0.4}Al_{0.55}Zr_{0.05}N$ (b), and $Ti_{0.39}Al_{0.51}Zr_{0.1}N$ (c) films after oxidation at 850 °C for 20 h. On top of the Zr-free $Ti_{0.48}Al_{0.52}N$ film, a multilayered, ~2 μm thick oxide scale composed of a dense Al_2O_3 outer-layer (~0.3 μm) and porous TiO_2 containing sub-layer can be identified with the assistance of EDX. Here, already some crack formation within the sub-layer can be observed, see Fig. 10a. The oxide scale on top of the lower Zr-containing film, $Ti_{0.4}Al_{0.55}Zr_{0.05}N$, is with 0.7 μm much thinner whereas that on the higher Zr-containing film, $Ti_{0.39}Al_{0.51}Zr_{0.1}N$, is with ~2.3 μm even thicker than that on $Ti_{0.48}Al_{0.52}N$, see Fig. 10b and c. Nevertheless, the oxide scales on both Zr-containing films are dense and uniform, without any layered structure or crack formation. EDX analyses confirm the uniform (within the detection limit) distribution of Ti, Al, Zr, and O. After oxidation at 950 °C for 20 h, the Zr-free film, $Ti_{0.48}Al_{0.52}N$, is completely oxidized, see Fig. 11a. The Zr-containing films, $Ti_{0.4}Al_{0.55}Zr_{0.05}N$ and $Ti_{0.39}Al_{0.51}Zr_{0.1}N$, still exhibit intact nitride layers underneath their oxide scales with thicknesses of ~1.0 and 3.4 μm, respectively, see Fig. 11b and c. These observations are in agreement with the XRD results

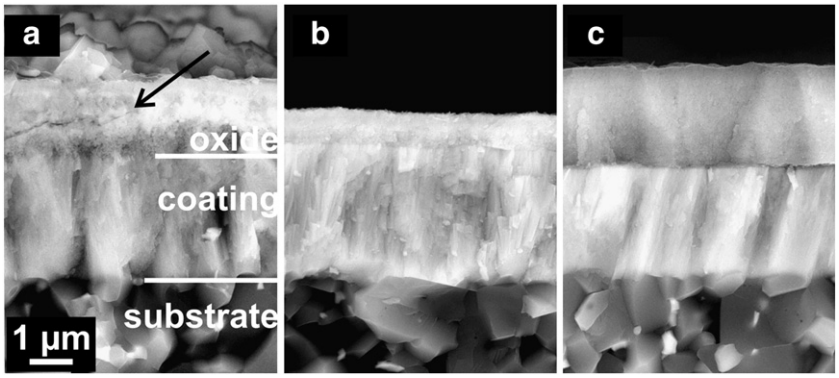

Fig. 10. SEM fracture cross-sectional images of (a) $Ti_{0.48}Al_{0.52}N$, (b) $Ti_{0.40}Al_{0.55}Zr_{0.05}N$, and (c) $Ti_{0.39}Al_{0.51}Zr_{0.10}N$ after isothermal oxidation at 850 °C for 20 h. The arrow in (a) indicates the formation of a crack.

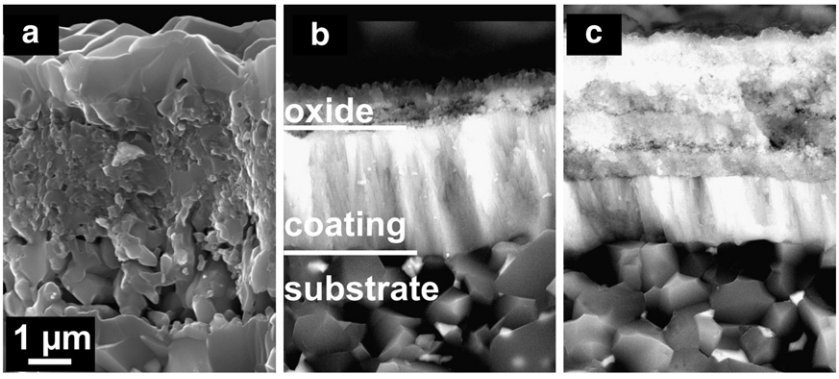

Fig. 11. SEM fracture cross-sectional images of (a) $Ti_{0.48}Al_{0.52}N$, (b) $Ti_{0.40}Al_{0.55}Zr_{0.05}N$, and (c) $Ti_{0.39}Al_{0.51}Zr_{0.10}N$ after isothermal oxidation at 950 °C for 20 h.

presented in Fig. 10 and clearly suggest that the addition of ~5% ZrN to $Ti_{1-x}Al_xN$ yields optimized oxidation resistance.

4. Summary and conclusions

Here, we present a detailed study on the effect of Zr incorporation on structural, mechanical and thermal properties of $Ti_{1-x}Al_xN$ thin films prepared by reactive magnetron sputtering. All films with compositions of $Ti_{0.48}Al_{0.52}N$, $Ti_{0.40}Al_{0.55}Zr_{0.05}N$, $Ti_{0.39}Al_{0.51}Zr_{0.10}N$, $Ti_{0.36}Al_{0.47}Zr_{0.17}N$, and $Ti_{0.34}Al_{0.37}Zr_{0.29}N$ exhibit a single phase cubic NaCl-type structure in the as deposited state, which is in agreement with ab initio calculations. Addition of Zr to $Ti_{1-x}Al_xN$ results in an increased hardness, where the maximum value of ~38 GPa is obtained for $Ti_{0.40}Al_{0.55}Zr_{0.05}N$.

During annealing in vacuum, the supersaturated matrix phase $Ti_{1-x-z}Al_xZr_zN$ decomposes to form Al-depleted and Al-enriched domains which cause an increase in hardness. Further annealing above 1000 °C results in the formation of w-AlN and hence a decreased hardness. Zirconium is very effective in influencing the age-hardening as it promotes the formation of cubic domains but retards the formation of w-AlN. Consequently, the hardness increases to values above ~35 GPa already after annealing at 700 °C and stays above ~35 GPa even after annealing to 1100 °C. The 5% ZrN containing layer, $Ti_{0.40}Al_{0.55}Zr_{0.05}N$, exhibits the best results of the films investigated. Its hardness increases from the as deposited value of ~38 GPa to ~42 GPa with $T_a = 1000$ °C and ~40 GPa with $T_a = 1100$ °C. In addition to the improvement of the age-hardening behavior of $Ti_{1-x}Al_xN$ by alloying with Zr, also their oxidation resistance increases. Zirconium promotes the formation of a dense oxide scale and thereby retards its growth rate. Also here, the best results are obtained for $Ti_{0.40}Al_{0.55}Zr_{0.05}N$, which shows even after annealing in air at 950 °C for 20 h only a ~1 μm thick oxide scale on top of the otherwise still intact layer.

Based on the results presented, we can conclude that the coating $Ti_{0.40}Al_{0.55}Zr_{0.05}N$ which contains only 5% Zr at the metal sublattice exhibits the best performance during hardness measurements in the as deposited state and after thermal annealing up to 1100 °C as well as during oxidation tests for 20 h at 850 and 950 °C.

Appendix A

Table A1
Arrangement of $3\times3\times2$ supercells used for the calculation of the cubic phases. The fractional coordinates are expressed in a cell with lattice vectors $a_1 = (1.5, 1.5, 0)$, $a_2 = (0, 1.5, 1.5)$, $a_3 = (1, 0, 1)$. Only atoms on the metallic sublattice are listed. The positions given here correspond to the starting configurations before any relaxation took place. Atoms marked with * and # were substituted by Zr in the supercells representing quaternary alloys with $z = 5.6\%$ and $z = 11.1\%$, respectively.

Fractional coordinate			Al content on the metallic sublattice															
x	*y*	*z*	0.056	0.111	0.167	0.222	0.278	0.333	0.389	0.444	0.500	0.556	0.611	0.667	0.722	0.778	0.833	0.889	0.944
0.000	0.000	0.000	Ti	Ti*#	Ti	Ti*#	Ti	Al	Ti	Al	Al	Ti*#	Al	Al	Al	Ti	Al	Al	Al
0.000	0.000	0.500	Ti	Ti	Ti	Ti	Ti	Ti*#	Al	Al	Al	Ti	Al	Al	Al	Al	Al	Al	Al
0.000	0.333	0.000	Ti	Ti	Ti	Al	Al	Ti	Ti	Al	Ti	Ti	Al	Ti*#	Al	Al	Al	Al	Al
0.000	0.333	0.500	Al	Al	Ti	Ti	Ti	Ti	Ti	Al	Al	Ti	Al	Ti	Al	Al	Al	Al	Al
0.000	0.667	0.000	Ti	Ti	Ti	Ti	Ti	Ti	Al	Ti*#	Ti	Al	Ti	Al	Al	Ti	Al	Ti	Al
0.000	0.667	0.500	Ti	Ti	Ti	Ti	Ti	Ti	Ti	Ti	Ti*#	Al	Ti*	Al	Al	Ti#	Ti*	Al	Al
0.333	0.000	0.000	Ti	Ti#	Ti	Ti	Ti	Ti	Ti	Ti	Al	Al	Al	Al	Al	Al	Al	Al	Al
0.333	0.000	0.500	Ti	Ti	Al	Al	Al	Al	Ti	Ti	Ti	Al	Al	Al	Al	Al	Ti	Al	Al
0.333	0.333	0.000	Ti	Ti	Ti	Ti	Ti	Ti#	Al	Ti	Al	Al	Al	Al	Al	Al	Ti	Al	Al
0.333	0.333	0.500	Ti	Ti	Ti	Ti	Ti	Ti	Al	Al	Ti	Ti#	Ti	Al	Ti*	Al	Al	Al	Al
0.333	0.667	0.000	Ti	Ti	Ti	Ti	Ti	Al	Ti	Ti	Ti	Al	Ti	Ti	Ti	Al	Al	Al	Al
0.333	0.667	0.500	Ti	Ti	Ti	Ti#	Ti	Ti	Al	Ti	Al	Al	Al	Ti	Ti	Al	Al	Al	Al
0.667	0.000	0.000	Ti	Ti	Ti	Al	Al	Al	Al	Ti#	Al	Al	Ti	Al	Ti	Al	Al	Al	Al
0.667	0.000	0.500	Ti	Ti	Ti	Al	Ti	Ti	Ti	Ti	Al	Al	Al	Al	Al	Al	Al	Ti	Al
0.667	0.333	0.000	Ti	Ti	Ti	Ti	Ti	Ti	Ti	Al	Al	Ti	Ti	Al	Al	Al	Al	Al	Al
0.667	0.333	0.500	Ti	Ti	Al	Ti	Al	Al	Ti	Ti	Ti	Al	Al	Ti#	Al	Ti#	Al	Al	Ti
0.667	0.667	0.000	Ti	Al	Al	Ti	Al	Ti	Ti	Al	Ti#	Ti	Al	Ti	Al	Al	Al	Al	Al
0.667	0.667	0.500	Ti	Ti	Ti	Ti	Ti	Al	Al	Al	Ti	Ti	Ti	Al	Ti	Al	Al	Al	Al

Table A2
Arrangement of $2\times2\times2$ supercells used for the calculation of the wurtzite phases. The fractional coordinates are expressed in a cell with lattice vectors $a_1 = (1, 1.73, 0)$, $a_2 = (1, -1.73, 0)$, $a_3 = (0, 0, 3.2)$. Only atoms on the metallic sublattice are listed. The positions given here correspond to the starting configurations before any relaxation took place. Atoms marked with * and # were substituted by Zr in the supercells representing quaternary alloys with $z = 6.25\%$ and $z = 12.5\%$, respectively.

Fractional coordinates			Al content on the metallic sublattice							
x	*y*	*z*	0.250	0.500	0.563	0.625	0.688	0.750	0.875	0.938
0.167	0.333	0.000	Ti*#	Ti*	Ti#	Ti*	Al	Al	Al	Al
0.167	0.333	0.500	Ti	Ti	Al	Al	Ti	Al	Ti	Ti
0.167	0.833	0.000	Ti	Al	Al	Al	Al	Ti#	Al	Al
0.167	0.833	0.500	Ti	Al	Ti#	Al	Ti	Al	Al	Al
0.333	0.167	0.250	Ti	Ti	Al	Ti	Ti*	Al	Al	Al
0.333	0.167	0.750	Ti	Ti#	Ti*	Al	Al	Al	Al*	Al
0.333	0.667	0.250	Al	Al	Al	Ti#	Al	Ti	Al	Al
0.333	0.667	0.750	Ti	Al	Al	Ti#	Al	Al	Al	Al
0.667	0.333	0.000	Ti	Ti	Al	Al	Al	Al	Al	Al
0.667	0.333	0.500	Al	Al	Ti	Al	Al	Ti#	Al	Al
0.667	0.833	0.000	Al	Ti	Al	Al	Al	Al	Al	Al
0.667	0.833	0.500	Ti	Al	Al	Ti	Al	Al	Al	Al
0.833	0.167	0.250	Al	Ti#	Ti	Al	Al	Al	Al	Al
0.833	0.167	0.750	Ti#	Al	Ti	Al	Al	Al	Ti	Al
0.833	0.667	0.250	Ti	Ti	Al	Ti	Ti	Ti	Al	Al
0.833	0.667	0.750	Ti	Al	Ti	Al	Ti	Al	Al	Al

Table A3
Warren–Cowley short range order parameters for the SQS cells used in this work (Tables A1 and A2). The shells correspond to nearest distances between atoms on the metallic sublattice.

Cubic B1						Wurtzite B4					
Shell						Shell					
Al content	1	2	3	4	5	Al content	1	2	3	4	5
0.056	−0.059	−0.059	−0.059	0.118	−0.059	0.250	0.000	−0.111	0.000	−0.333	0.000
0.111	−0.125	0.250	−0.125	0.063	0.063	0.500	−0.074	−0.037	0.000	0.037	−0.111
0.167	−0.133	0.067	0.000	0.000	0.000	0.563	−0.016	−0.101	−0.016	−0.270	−0.016
0.222	−0.071	0.036	−0.045	0.036	−0.071	0.625	−0.067	−0.067	−0.067	−0.067	−0.067
0.278	−0.062	−0.108	0.031	0.031	−0.154	0.688	−0.067	−0.067	0.127	0.127	−0.067
0.333	−0.042	0.000	−0.083	0.000	0.000	0.750	0.000	−0.111	0.000	−0.333	0.000
0.389	−0.052	−0.091	−0.032	−0.013	−0.013	0.875	0.048	−0.143	−0.143	−0.143	0.048
0.444	−0.088	−0.013	0.004	0.090	−0.105	0.938	−0.067	−0.067	−0.067	−0.067	−0.067
0.500	−0.074	−0.037	0.000	0.037	−0.111						
0.556	−0.088	−0.013	0.004	0.090	−0.105						
0.611	−0.091	−0.091	−0.013	0.052	0.065						
0.667	−0.083	−0.083	0.000	0.000	−0.042						
0.722	−0.108	−0.015	0.008	−0.015	−0.015						
0.778	−0.071	0.036	−0.045	0.036	−0.071						
0.825	−0.125	0.250	−0.125	0.063	0.063						
0.883	−0.133	0.067	0.000	0.000	0.000						
0.944	−0.059	−0.059	−0.059	0.118	−0.059						

Acknowledgments

The START project (Y371) of the Austrian Science Fund FWF is gratefully acknowledged by the authors. Li Chen thanks the National Natural Science Foundation for Youth of China (Grant No. 51001120) and the postdoctoral foundation of China (Grant No. 20100470060). Yong Du acknowledges Creative Research Group of National Natural Science Foundation of China (Grant No. 51021063).

References

[1] S. PalDey, S.C. Deevi, Mater. Sci. Eng. A. 342 (2003) 58.
[2] L. Hultman, Vacuum 57 (2000) 1.
[3] L. Chen, M. Moser, Y. Du, P.H. Mayrhofer, Thin Solid Film 517 (2009) 6635.
[4] A. Hörling, L. Hultman, M. Oden, J. Sjölen, L. Karlsson, Surf. Coat. Technol. 191 (2005) 384.
[5] P.H. Mayrhofer, A. Hörling, L. Karlsson, J. Sjölen, T. Larsson, C. Mitterer, L. Hultman, Appl. Phys. Lett. 83 (2003) 2049.
[6] L. Chen, Y. Du, P.H. Mayrhofer, S.Q. Wang, J. Li, Surf. Coat. Technol. 202 (2008) 5158.
[7] P.H. Mayrhofer, F.D. Fischer, H.J. Böhm, C. Mitterer, J.M. Schneider, Acta. Mater. 55 (2007) 1441.
[8] P.H. Mayrhofer, H. Willmann, A.E. Reiter, Surf. Coat. Technol. 202 (2008) 4935.
[9] H. Holleck, Surf. Coat. Technol. 36 (1988) 151.
[10] R. Lamni, R. Sanjinés, M. Parlinska-Wojtan, A. Karimi, F. Lévy, J. Vac. Sci. Technol. A. 23 (2005) 593.
[11] C. Höglund, J. Birch, B. Alling, J. Bareño, Z. Czigány, P.O.Å. Persson, G. Wingqvist, A. Zukauskaite, L. Hultman, J. Appl. Phys. 107 (2010) 123515.
[12] P.H. Mayrhofer, D. Music, J.M. Schneider, J. Appl. Phys. 100 (2006) 094906.
[13] P.H. Mayrhofer, D. Music, J.M. Schneider, Appl. Phys. Lett. 88 (2006) 071922.
[14] P.H. Mayrhofer, F.D. Fischer, H.J. Böhm, C. Mitterer, J.M. Schneider, Acta. Mater. 55 (2007) 1441.
[15] K. Kutschej, P.H. Mayrhofer, M. Kathrein, P. Polcik, C. Mitterer, Surf. Coat. Technol. 188–189 (2004) 358.
[16] L. Chen, Y. Du, S.Q. Wang, J. Li, Int. J. Refract. Met. Hard. Mater. 25 (2007) 400.
[17] H. Hasegawa, Y. Kimura, T. Suzuki, Surf. Coat. Technol. 132 (2000) 76.
[18] D. McIntyre, J.E. Greene, G. Hakansson, J.E. Sundgren, W.D. Münz, J. Appl. Phys. 67 (1990) 1542.
[19] F. Vaz, L. Rebouta, M. Andritschky, M.F. Silva, J.C. Soares, J. Eur. Ceram. Soc. 17 (1997) 1971.
[20] R. Rachbauer, E. Stergar, S. Massl, M. Moser, P.H. Mayrhofer, Scrip. Mater. 61 (2009) 725.
[21] R. Sanjinés, C.S. Sandu, R. Lamni, F. Lévy, Surf. Coat. Technol. 200 (2006) 6308.
[22] L. Rogström, L.J.S. Johnson, M.P. Johansson, M. Ahlgren, L. Hultman, M. Odén, Scrip. Mater. 62 (2010) 739.
[23] S.H. Sheng, R.F. Zhang, S. Veprek, Acta. Mater. 56 (2008) 968.
[24] P.H. Mayrhofer, R. Rachbauer, D. Holec, Scrip. Mater. 63 (2010) 807.
[25] M. Pfeiler, G.A. Fontalvo, J. Wagner, K. Kutschej, M. Penoy, Tribol. Lett. 30 (2008) 91.
[26] M. Moser, P.H. Mayrhofer, H. Clemens, Intermetallics 16 (2008) 1206.
[27] M. Moser, P.H. Mayrhofer, Scrip. Mater. 57 (2007) 357.
[28] M. Moser, P.H. Mayrhofer, Materials 3 (2010) 1573.
[29] K. Wasa, S. Hayakawa, Thin Solid Films 10 (1972) 367.
[30] O. Knotek, M. Böhmer, T. Leyendecker, F. Jungblut, Mater. Sci. Eng. A. 105–106 (1988) 481.
[31] P.H. Mayrhofer, M. Geier, C. Löcker, L. Chen, Int. J. Mater. Res. 8 (2009) 1052.
[32] Powder Diffraction File JCPDS-International Center for Diffraction Data Swarthmore 2001 Cards 25-1133 (w-AlN), 38-1420 (c-TiN), 31-1493 (c-ZrN), 21-1272 (a-TiO2), 21-1276 (r-TiO2), 46-1212 (α-Al2O3), 1-075-1739 (o-Zr0.33Ti0.67O2).
[33] W.C. Oliver, G.M. Pharr, J. Mater. Res. 7 (1992) 1564.
[34] P.H. Mayrhofer, C. Mitterer, Surf. Coat. Technol. 133–134 (2000) 131.
[35] G. Kresse, Furthmüller, Phys. Rev. B. 54 (1996) 11169.
[36] G. Kresse, D. Joubert, Phys. Rev. B. 59 (1999) 1758.
[37] S.H. Wei, L.G. Ferreira, J.E. Bernard, A. Zunger, Phys. Rev. B. 42 (1990) 9622.
[38] D. Holec, Multi-Scale Modelling of III-Nitrides: Selected Topics from Dislocations to the Electronic Structure, VDM, Verlag, 2010.
[39] B. Alling, A.V. Ruban, A. Karimi, O.E. Peil, S.I. Simak, L. Hultman, I.A. Abrikosov, Phys. Rev. B 75 (2007) 045123.
[40] D. Holec, R. Franz, P.H. Mayrhofer, C. Mitterer, J. Phys. D: Appl. Phys. 43 (2010) 145403.
[41] D. Holec, R. Rachbauer, D. Kiener, P.D. Cherns, P.M.F.J. Costa, C. McAleese, P.H. Mayrhofer, C.J. Humphreys, Phys. Rev. B 83 (2011) 165122.
[42] H. Hiroyuki, K. Ayako, S. Tetsuya, Surf. Coat. Technol. 132 (2000) 76.
[43] A. Hörling, J. Sjölen, H. Willmann, T. Larsson, M. Odén, L. Hultman, Thin Solid Films 516 (2008) 6421.